Analyzing the Well-Interference Phenomenon in the Eagle Ford Shale/Austin Chalk Production System With a Comprehensive Compositional Reservoir Model

Article *in* SPE Reservoir Evaluation & Engineering · September 2018

DOI: 10.2118/191381-PA

CITATIONS
34

READS
464

6 authors, including:

Hewei Tang
Lawrence Livermore National Laboratory
31 PUBLICATIONS **519** CITATIONS
SEE PROFILE

Bicheng Yan
King Abdullah University of Science and Technology
112 PUBLICATIONS **1,312** CITATIONS
SEE PROFILE

Zhi Chai
Texas A&M University
20 PUBLICATIONS **468** CITATIONS
SEE PROFILE

Lihua Zuo
Texas A&M University - Kingsville
43 PUBLICATIONS **1,152** CITATIONS
SEE PROFILE

Analyzing the Well-Interference Phenomenon in the Eagle Ford Shale/Austin Chalk Production System With a Comprehensive Compositional Reservoir Model

Hewei Tang, Bicheng Yan (currently with Sanchez Oil and Gas), **Zhi Chai, Lihua Zuo,** and **John Killough,** Texas A&M University; and **Zhuang Sun,** University of Texas at Austin

Summary

Well interference is a common phenomenon in unconventional-reservoir development. The completion and production of infill wells can lead to either positive or negative well-interference impacts on the existing producers. Many researchers have investigated the well-interference phenomenon; however, few of them attempted to apply rigorous simulation methods to analyze both positive and negative well-interference effects, especially in two different formations. In this work, we develop a comprehensive compositional reservoir model to study the well-interference phenomena in the Eagle Ford Shale/Austin Chalk production system. The reservoir model considers capillary pressure in the vapor/liquid-equilibrium (VLE) equation (nanopore-confinement effect), and applies the embedded discrete-fracture model (EDFM) for dynamic fracture modeling. We also include a multisegment-well model to characterize the wellbore-crossflow effect introduced by fracture hits. The simulation results indicate that negative well-interference impact is much more common in the production system. With a smaller permeability difference, the hydraulic-fracturing effect can lead to a positive well-interference period of several hundred days. The nanopore-confinement effect in the Eagle Ford Shale can contribute to the negative well-interference effect. We also analyze the impact of other factors such as initial reservoir pressure, matrix porosity, initial water saturation, and the natural-fracture system on the well performance. Our work provides valuable insights into dynamic well performance under the impact of well interference.

Introduction

Well-Interference Phenomenon. Massive and complex hydraulic fractures created by drilling multiple wellpads and multistage hydraulic fracturing lead to the successful development of unconventional reservoirs (He et al. 2017; Liu et al. 2018; Tang et al. 2017b). However, as well spacing decreases, the extensive fractures from adjacent wells also increase the chance of "fracture hits" and result in well interference (Sahai et al. 2015; Awada et al. 2016).

Previous studies have varying definitions for fracture hits. We subdivide these definitions into two categories based on the places where fracture hits happen. The first category of fracture hit happens in the near-wellbore region of parent wells. It can result in the removal of considerable amounts of proppant in hydraulic fractures or wellbore failures (Fjar et al. 2008). Therefore, this kind of fracture hit often leads to mild or severe negative impacts on the production of existing parent wells (Marongiu-Porcu et al. 2016). To simulate this kind of well interference, Marongiu-Porcu et al. (2016) introduced a permeability reduction to the fracture-hit regions around the parent well, as illustrated in **Fig. 1.**

The second category of fracture hits happens in the stimulated reservoir volume (SRV) of parent wells. The feature of this kind of fracture hit is the creation of hydraulic connections as the fractures of infill wells propagate and hit the fractures of parent wells. This kind of fracture hit leads to either a positive or a negative impact on the production of existing parent wells, with the negative impact being much more common on the basis of field observations (Ajani and Kelkar 2012; Kurtoglu and Salman 2015). This paper focuses on simulating the production impacts of the second category of fracture hits.

Some researchers have quantitatively analyzed the impact of well interference on shale-reservoir development. Sahai et al. (2015) applied a rate-transient-analysis (RTA) model combined with the fracture-area loss theory to explain the sudden productivity decline of parent wells. Jia et al. (2017) investigated the flow behavior inside the interconnected fractures through a Laplace-domain hybrid model. The model dynamically coupled the analytically solved matrix flow with the numerically solved fracture flow. Both RTA-based methods and semianalytical methods can lead to computationally efficient solutions to the problems. However, a full numerical simulation is still required to account for the heterogeneity and multiphase flow in reservoirs. Yu et al. (2018) simulated the production of multiple wells under well interference by use of a compositional reservoir model. Their model was capable of characterizing the complex geometry of hydraulic and natural fractures. However, they only presented the cumulative production of several interference wells in a single reservoir, and did not investigate the impact of well interference on existing producers. We consider this investigation to be important, especially for parent wells and infill wells completed in different formations, such as the Eagle Ford Shale and Austin Chalk, because the wells very likely belong to different operators.

Eagle Ford Shale and Austin Chalk Formations. The Eagle Ford Shale Formation is in the Western Gulf Basin, south Texas. It overlies the Buda Limestone and underlies the Austin Chalk. The Eagle Ford Shale is a self-sourced reservoir with seals. Hentz and Ruppel (2010) divided the Eagle Ford Shale Formation into the Lower Eagle Ford and the Upper Eagle Ford. The Lower Eagle Ford, which is present throughout the whole area of the play, has higher gamma ray and resistivity responses, reflecting its richness in organic matter. However, the Upper Eagle Ford is restricted to the west region of the play, and it has more carbonate. The elevation of the Eagle Ford

Original SPE manuscript received for review 8 January 2018. Revised manuscript received for review 16 May 2018. Paper (SPE 191381) peer approved 23 May 2018.

Shale Formation decreases from 3,500 ft subsea to 14,000 ft subsea southwestward. As the basin gets deeper and more thermally mature, the Eagle Ford fluids exhibit an evolution from oil to gas condensate and then to dry gas (Energy Information Agency 2010). The reservoir properties also vary significantly across the play, with porosity ranging between 2 and 10% and permeability ranging between 0.1 and 1,000 nd (Walls and Sinclair 2011; Siripatrachai et al. 2017). Commercial production in the Eagle Ford Shale was first obtained in 2008 with a combination of horizontal drilling and hydraulic fracturing (Tunstall 2015).

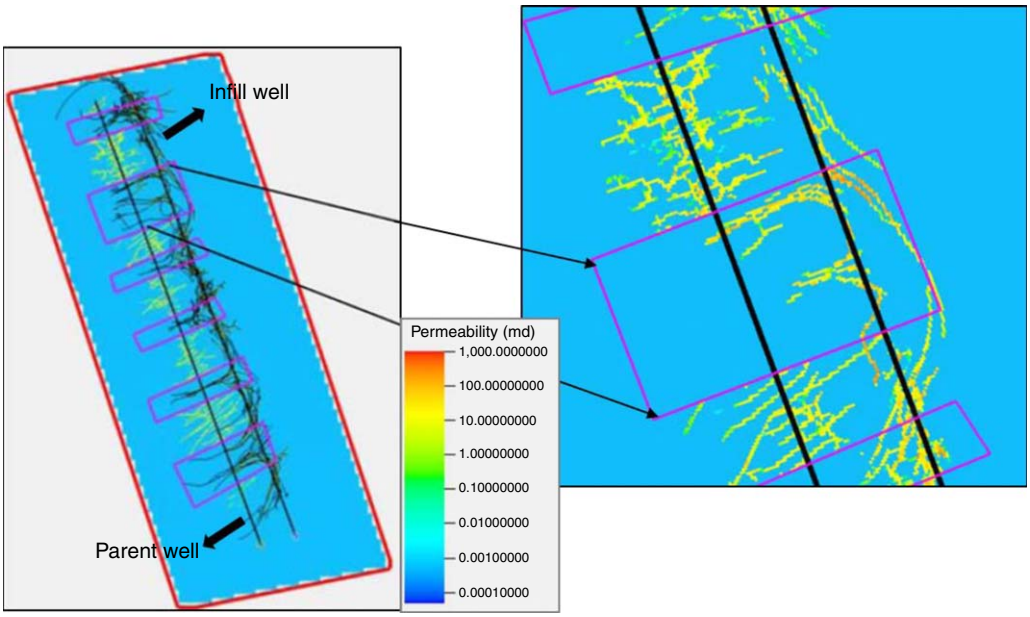

Fig. 1—Illustration of parent-well permeability reduction caused by fracture hits. Purple rectangles represent the fracture-hit areas. Black contours are fractures of the infill well. The right-hand figure shows the resulting permeability field after permeability reduction (modified after Marongiu-Porcu et al. 2016).

The Austin Chalk Formation extends from southern Louisiana to south-central Texas. The Austin Chalk is a tight oil reservoir with the Eagle Ford Shale as its source rock. Hydrocarbons sourced from the Eagle Ford Shale charge the Austin Chalk reservoirs through vertical migration pathways formed by fracture networks (Pearson 2010). The matrix porosity of the Austin Chalk reservoir is between 3 and 10%, and the matrix permeability is between 0.03 and 1.27 md (Hovorka 1998). The Austin Chalk has been a target of numerous horizontal wells since the late 1980s (Martin et al. 2011).

Martin et al. (2011) studied the production system formed by the Austin Chalk and the Eagle Ford Shale from the perspectives of geological features and production activities. They proved the possibility that the two formations form a single hydrocarbon system. Okeahialam et al. (2017) investigated the well-production performance of the Eagle Ford Shale play in Gonzales and Lavaca counties. In this region, the Upper Eagle Ford has pinched out, and the Austin Chalk is directly above the Lower Eagle Ford. They observed that the oil-production rate of a parent well in the Austin Chalk Formation increased significantly after an infill well in the Eagle Ford Shale started to produce, as shown in **Fig. 2.** This field case reveals that, although the positive well-interference effect is not common, it does happen in the Eagle Ford Shale/Austin Chalk production system.

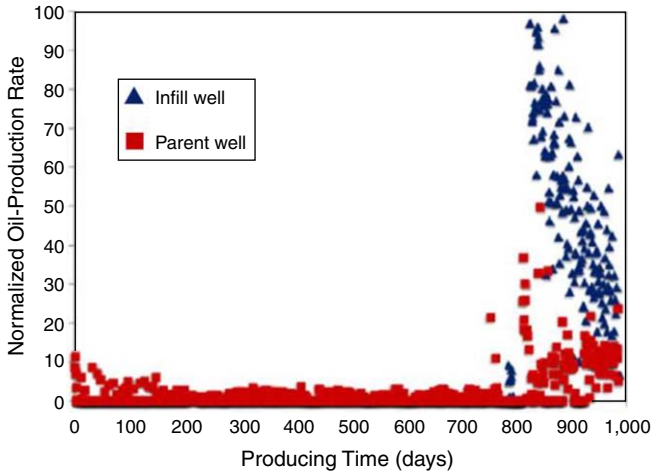

Fig. 2—Normalized production rates of a parent well in the Austin Chalk Formation and an infill well in the Eagle Ford Shale Formation (Okeahialam et al. 2017).

The objective of this work is to investigate the factors that may lead to negative or positive well-interference effects from the perspective of reservoir simulation. An in-house compositional reservoir simulator is applied to study the dynamic rate alteration of a parent well in the Austin Chalk Formation that is influenced by an infill well in the Eagle Ford Shale Formation. We apply an EDFM within the compositional reservoir model to simulate the dynamic-fracture-network changes introduced by infill wells. The model is validated with a commercial reservoir simulator. We design different well-interference scenarios to evaluate the impacts of reservoir permeability, nanopore confinement, and hydraulic fracturing on the well interference between parent and infill wells. This work analyzes the well-interference effects in two formations with significant property differences for the first time.

Methodology

Compositional Reservoir Model. We consider three-phase (oil, gas, and water) Darcy flow in the subsurface isothermal porous media. For each hydrocarbon component c in oil and gas phases, a mass-conservation equation is given in Eq. 1. Similarly, Eq. 2 expresses the mass-conservation equation in the water phase. We assume that water is inertial and does not present in the oil and gas phases. The primary variables associated with these two equations are N_c and N_w, with definitions that are given by Eqs. 3 and 4 (Valbuena Olivares 2015; Yan 2017):

$$\nabla\left[kA\left(x_c\frac{k_{ro}}{\mu_o}\nabla\psi_o+y_c\frac{k_{rg}}{\mu_g}\nabla\psi_g\right)\right]=V_b\frac{\partial}{\partial t}(\phi N_c)-\sum_{\text{perf}}M_{c,p} \quad \ldots\ldots (1)$$

$$\nabla\left(kA\frac{k_{rw}}{\mu_w}\nabla\psi_w\right)=V_b\frac{\partial}{\partial t}(\phi N_w)-\sum_{\text{perf}}M_{w,p} \quad \ldots\ldots (2)$$

$$N_c=S_o\rho_{mo}x_c+S_g\rho_{mg}y_c \quad \ldots\ldots (3)$$

$$N_w=S_w\rho_{mw}, \quad \ldots\ldots (4)$$

where V_b is the bulk rock volume, A is the cross-sectional area, x_c and y_c are the mole fractions of component c in oil and gas phases, k is the absolute permeability, $k_{r\alpha}$ ($\alpha=o, g, w$) is the phase relative permeability, ψ_α ($\alpha=o, g, w$) is the phase potential considering pressure and gravitational forces acting on the phase, S_α ($\alpha=o, g, w$) is the phase saturation, $\rho_{m\alpha}$ is the molar density of phase α, and $M_{c,p}$ and $M_{w,p}$ are the net molar rates of component c and water from each perforation. Another primary equation is a volume constraint ensuring that total fluid volume of each phase ($V_{\alpha,i}$) is equal to the pore volume (PV) (PV_i) of each reservoir grid i. The associated primary variable is the oil-phase pressure (P_o),

$$PV_i=\sum\nolimits_{\alpha=o,g,w}V_{\alpha,i}. \quad \ldots\ldots (5)$$

The compositional reservoir model is spatially discretized on the basis of the control-volume finite-difference method proposed by Cao (2002) with a two-point flux approximation. For time discretization, a fully implicit scheme is applied.

Multisegment-Wellbore Model. We apply the multisegment-wellbore model to account for the wellbore crossflow in the well-interference phenomenon. The multisegment-wellbore model, which was first introduced by Stone et al. (1989), discretizes the wellbore into segments and solves the well equations simultaneously with the reservoir equations. In our application, we only discretize the horizontal lateral of the wellbore that is based on the fracture stages. This practice can help us accurately track the pressure of each perforation. For each wellbore segment, we honor the mass conservation for each component and water, as shown in Eqs. 6 and 7. We also solve a pressure-drop equation, as shown in Eq. 8 (Tang et al. 2017a):

$$\nabla\left[A\left(S_{o,\text{seg}}x_c\rho_{mo,\text{seg}}u_{so}+S_{g,\text{seg}}y_c\rho_{mg,\text{seg}}u_{sg}\right)\right]=V_{\text{seg}}\frac{\partial}{\partial t}(N_c)+M_{c,p} \quad \ldots\ldots (6)$$

$$\nabla(AS_{w,\text{seg}}\rho_{mw,\text{seg}}u_{sw})=V_{\text{seg}}\frac{\partial}{\partial t}(N_w)+M_{w,p} \quad \ldots\ldots (7)$$

$$\frac{\partial P_p}{\partial z}+\frac{\partial\rho_m u_m^2}{\partial z}+\frac{f_f\rho_m u_m|u_m|}{2d_{\text{in}}}+\rho_m g\cos\theta=0, \quad \ldots\ldots (8)$$

where V_{seg} is segment volume, $\rho_{m\alpha,\text{seg}}$ and $S_{\alpha,\text{seg}}$ ($\alpha=o, g, w$) are the phase molar density and the phase saturation at perforated well segments, $u_{s\alpha}$ ($\alpha=o, g, w$) are superficial velocities of each phase, and u_m is the mixture fluid velocity. We assume homogeneous flow inside the wellbore, where $u_{so}=u_{sg}=u_{sw}=u_m$. P_p is the wellbore pressure at perforation p. ρ_m is the mixture density given by $\rho_m=\alpha_o\,\rho_o+\alpha_g\,\rho_g+\alpha_w\,\rho_w$. f_f is the friction factor, and d_{in} is the pipe inside diameter. The net molar rates $M_{c,p}$ and $M_{w,p}$ can be calculated as

$$M_{c,p}=WI[\lambda_o x_c(P_o-P_p)+\lambda_g y_c(P_g-P_p)] \quad \ldots\ldots (9)$$

$$M_{w,p}=WI[\lambda_w(P_w-P_p)], \quad \ldots\ldots (10)$$

where WI is the well-geometry index, P_α ($\alpha=o, g, w$) is the phase pressure at perforated cells, and λ_α ($\alpha=o, g, w$) is the phase mobility, which is evaluated on the basis of the flow direction. For production scenario ($P_\alpha>P_p$), the phase mobility is evaluated at perforated cells,

$$\lambda_\alpha=k_{r\alpha}\frac{\rho_{m\alpha}}{\mu_\alpha}, \quad \ldots\ldots (11)$$

where μ_α is the phase viscosity. For the injection scenario ($P_\alpha<P_p$), the phase mobility is evaluated through the total mobility at perforated cells and the fluid properties at perforated well segments (Holmes 1983),

$$\lambda_\alpha=\left(\frac{k_{ro}}{\mu_o}+\frac{k_{rg}}{\mu_g}+\frac{k_{rw}}{\mu_w}\right)\rho_{m\alpha,\text{seg}}S_{\alpha,\text{seg}}. \quad \ldots\ldots (12)$$

If there are fracture hits between parent and infill wells, we can observe a rate jump of the parent well when the infill well starts to produce, which is because of the wellbore crossflow. The application of the multisegment-wellbore model allows the program to characterize this production scenario automatically.

VLE. Fluid properties of oil and gas phases are calculated through vapor/liquid flash calculations that are based on the equation of state (EOS). Component fugacity equilibrium (Eq. 10) and the Rachford-Rice Equation (Eq. 11) are solved together to obtain the equilibrium ratio (K_c) for each component and vapor mole fraction (f_v) (Yan et al. 2017; Zhang et al. 2017a),

$$K_c = \frac{\varphi_{c,l} p_l}{\varphi_{c,v} p_v} \quad \ldots\ldots (13)$$

$$\sum_{c=1}^{n_c} \frac{(K_c - 1) z_c}{1 + f_v (K_c - 1)} = 0, \quad \ldots\ldots (14)$$

where z_c is the overall mole fraction of component c, $\varphi_{c,l/v}$ is the liquid and vapor fugacity coefficient of component c, and $p_{l/c}$ is the liquid and vapor-phase pressure. The fugacity coefficient for each phase α ($\alpha = l, v$) is calculated with the Peng-Robinson EOS (Yan et al. 2017; Zhang et al. 2017a):

$$\ln(\varphi_{c,\alpha}) = \frac{b_c}{b}(Z_\alpha - 1) - \ln(Z_\alpha - B_\alpha) + \frac{A_\alpha}{2\sqrt{2}B_\alpha}\left\{\frac{b_c}{b} - \frac{1}{a}\left[2\sqrt{a_j}\sum_{c=1}^{n_c} x_c \sqrt{a_c}(1 - \kappa_{cj})\right]\right\} \ln\left[\frac{Z_\alpha + (1+\sqrt{2})B_\alpha}{Z_\alpha - (1-\sqrt{2})B_\alpha}\right]. \quad \ldots\ldots (15)$$

Appendix A lists the definition of each parameter. We combine the successive-substitution-iteration (SSI) method and the Newton-Raphson (NR) method to solve Eqs. 10 and 11. The solution from the SSI is applied as an initial guess for NR iteration to improve the convergence speed.

In traditional compositional reservoir models, liquid-phase pressure is assumed to be equal to the vapor-phase pressure, and Eq. 14 can be reduced to $K_c = \varphi_{c,l} / \varphi_{c,v}$. It is a valid assumption for conventional reservoirs, which have large PVs. However, for shale reservoirs, with pore sizes that are at nanoscale (Kou et al. 2017), it is no longer a reasonable assumption. The nanopores in a shale reservoir result in high capillary pressure and significant changes in fluid properties such as bubblepoint pressure, fluid densities, and viscosities (Nojabaei et al. 2013). Some researchers have reported that the high capillary pressure affects the well performance and the estimated ultimate recovery (EUR) of the reservoir (Siripatrachai et al. 2017; Zhang et al. 2017b).

EDFM. In this study, both the Austin Chalk and the Eagle Ford Shale are modeled as a single continuum. The permeability in the diffusivity equations (Eqs. 1 and 2) reflects both natural and matrix permeability without considering the flow between these two media. We model the hydraulic fractures explicitly with an EDFM. The EDFM is developed for Cartesian reservoir grids to achieve a higher computational efficiency for fracture modeling (Moinfar 2013). The fractures in the model are treated as additional quadrilateral plates, which are naturally discretized by the boundary of matrix grids (Jiang and Younis 2017). The model honors fluid flow through non-neighbor connections (NNCs) between fracture segments and matrix grids, between fracture segments in a single fracture, and between intersecting fractures. Transmissibility (T_{NNC}) of all three types of NNCs is generally expressed as (Chai et al. 2018)

$$T_{NNC} = \frac{k_{NNC} A_{NNC}}{d_{NNC}}, \quad \ldots\ldots (16)$$

where k_{NNC}, A_{NNC}, and d_{NNC} are the harmonic average of permeability, contact area, and distance between the two cells in the connection. The well index for wellbore-fracture connection is based on the Peaceman equation (Xu et al. 2017):

$$WI = \frac{2\pi k_f w_f}{\ln\left(\frac{0.14\sqrt{l^2 + h^2}}{r_w}\right)}, \quad \ldots\ldots (17)$$

where k_f and w_f are permeability and width of the fracture, l and h are length and height of the fracture segment, and r_w is the wellbore radius. For the simulation of well interference, the separate grid system of EDFM enables the convenient handling of the dynamic change in fracture networks resulting from the completion of infill wells.

Model Verification

A 3D synthetic reservoir model is set up to represent the Eagle Ford Shale/Austin Chalk production system **(Fig. 3).** The reservoir has a dimension of 3,000×1,000×300 ft and three equal-sized layers (100 ft) in the vertical direction. The top layer (Layer 1) represents the Austin Chalk Formation, and the bottom two layers (Layers 2 and 3) represent the Eagle Ford Shale Formation. A horizontal well (represented by black line) with four planar hydraulic fractures (represented by red lines) is completed in the Austin Chalk Formation. The half-length of the fractures is 250 ft. We assume that these fractures penetrate through Layer 1 with a height of 100 ft. **Table 1** lists all reservoir properties and well-control parameters of the model. We assume that the vertical permeability is equal to the horizontal permeability in the two formations. A separate study indicates that the vertical permeability does not influence the competitive drainage between parent and infill wells in the production system. We honor two production constraints simultaneously: One is a maximum production-rate control of 2,000 STB/D, and the other is a minimum bottomhole-pressure (BHP) control of 2,000 psia. Because most hydrocarbon in Austin Chalk is sourced from the Eagle Ford Shale, we assume that they share the same fluid compositions. We apply the five pseudocomponents for Eagle Ford Shale (CO_2, N_2–C_1, C_2–C_5, C_6–C_{10}, C_{11+}) reported by Yu et al. (2018), with molar fractions and properties that are listed in **Table 2.** The binary-interaction parameters among components are the same as those in the original publication. The relative permeability curves for matrix and fractures in Austin Chalk are shown in **Fig. 4** (Valbuena Olivares 2015). The Stone II (Stone 1973) method is applied to calculate the three-phase relative permeability. The capillary pressures between oil and water phases and between gas and oil phases in the Eagle Ford Shale layers are shown in **Fig. 5** (Siripatrachai et al. 2017). For the base case, we consider only the impacts of capillary pressure on flow behavior.

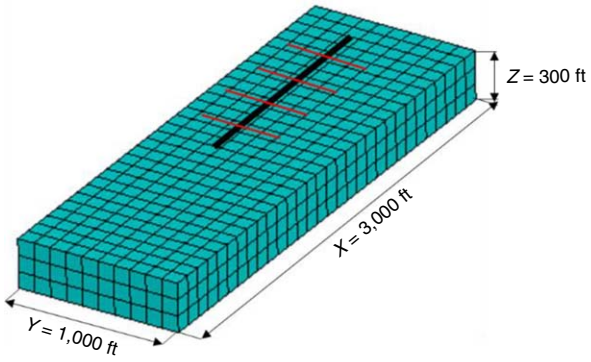

Fig. 3—3D layout of the synthetic reservoir model for verification.

Parameter	Value	Units
Initial reservoir pressure (Layer 1)	8,000	psi
Reservoir pressure gradient	0.45	psi/ft
Initial water saturation	0.3	–
Reservoir temperature	270	°F
Rock-matrix porosity	0.1	–
Rock-matrix permeability (Layer 1)	0.18	md
Rock-matrix permeability (Layers 2 and 3)	450	nd
Rock compressibility	4×10^{-6}	psi^{-1}
Fracture width	0.1	ft
Fracture porosity	0.3	–
Fracture permeability	1,000	md
Fracture half-length	250	ft
Wellbore diameter	0.5	ft
Maximum oil-production rate	2,000	STB/D
Minimum BHP	2,000	psia

Table 1—Parameters for the base case.

Component	Molar Fraction	Molar Weight	Acentric Factor	Critical Pressure (psia)	Critical Temperature (°F)	Critical Volume (ft^3/mol)
CO_2	0.2506	44.01	0.2250	1,069.86	87.89	1.506
N_2–C_1	0.2200	16.21	0.0084	664.84	–118.26	1.584
C_2–C_5	0.2000	52.02	0.1723	472.77	155.46	3.672
C_6–C_{10}	0.1300	103.01	0.2839	360.20	419.77	6.315
C_{11+}	0.1994	304.39	0.6716	222.20	1097.33	14.206

Table 2—Component properties for Eagle Ford Shale fluid (modified after Yu et al. 2018).

We validate the compositional reservoir model with EDFM against a commercial reservoir simulator applying the local-grid-refinement (LGR) method for fracture modeling. To resemble the actual production process, the well is produced under a maximum oil-production rate constraint of 2,000 STB/D and a minimum BHP of 2,000 psi. Simulation results of BHP, oil-production rate, and gas-production rate are compared in **Figs. 6a through 6c.** All the results are in excellent agreement, which demonstrates the reliability of our compositional model and the EDFM fracture-modeling technique.

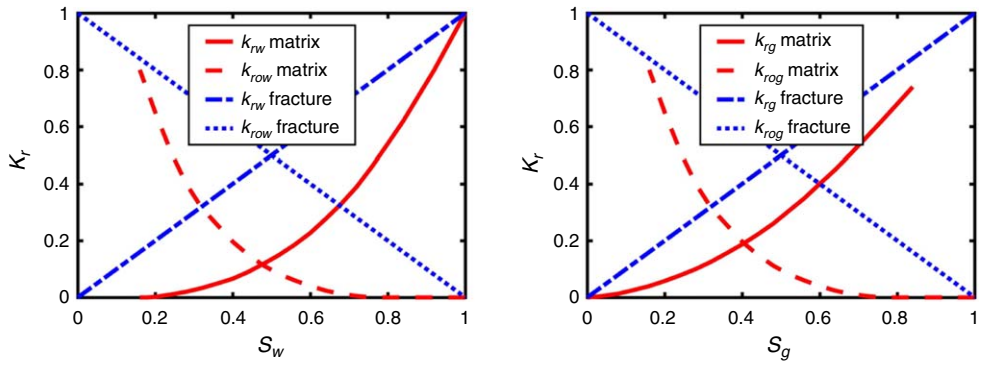

Fig. 4—Relative permeability curves for rock matrix and fractures in the Austin Chalk (Valbuena Olivares 2015).

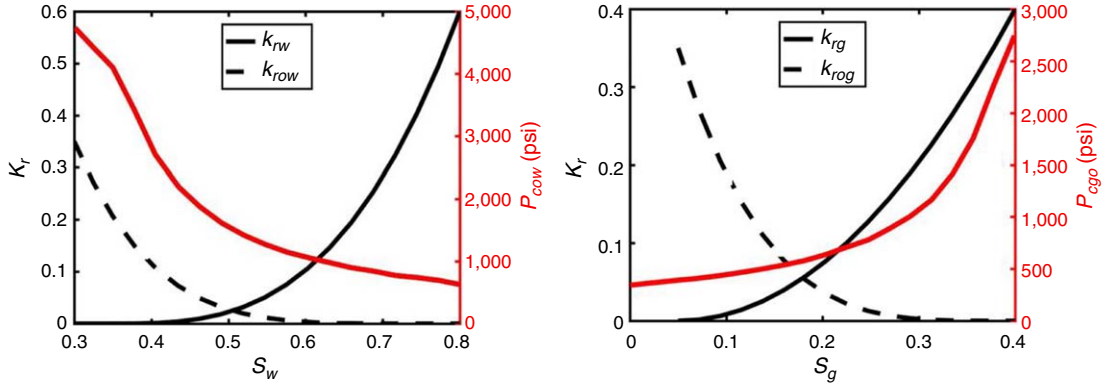

Fig. 5—Relative permeability curves and capillary pressure curves for rock matrix in the Eagle Ford Shale (Agboada and Ahmadi 2013).

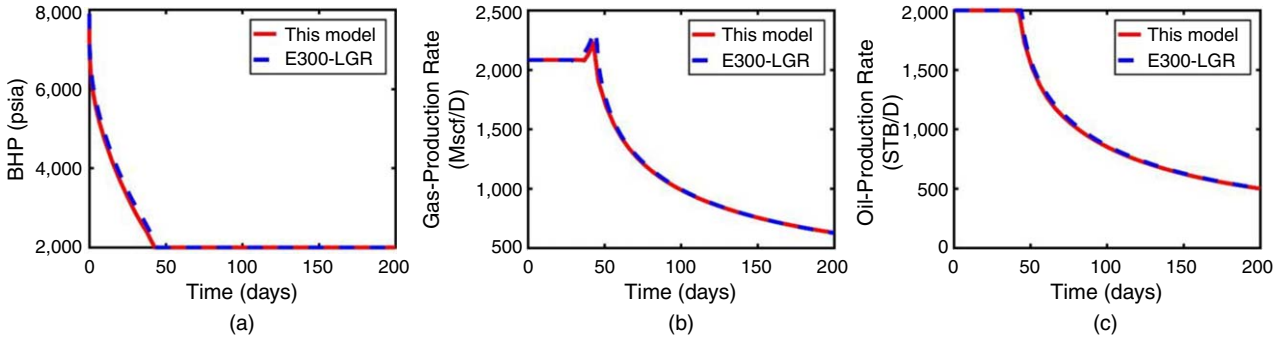

Fig. 6—Result comparison of BHP and oil- and gas-production rates between this model and commercial reservoir simulator.

Case Studies

Effect of Different Well-Interference Scenarios. To evaluate the impact of infill wells in the Eagle Ford Shale Formation on the production of parent wells in the Austin Chalk Formation, we design three different well-interference cases shown in **Fig. 7.** For all three cases, the parent well in the Austin Chalk layer is the same as that in the base case, and the infill well in the Eagle Ford Shale layer is completed in the third layer of the synthetic model. The two wells in the Austin Chalk Formation and the Eagle Ford Shale Formation are placed such that they are staggered vertically. All existing fractures of the parent well are marked as red lines, and the new fractures of the infill well are marked as green lines. The infill well has nine stages of fractures. In Case 1, nine planar fractures of the infill well penetrate through Layers 2 and 3 with a height of 200 ft. Four of these fractures directly hit the four planar fractures of the parent well at Row 5 and Row 6 in the *y*-direction of the synthetic model. In Case 2, the first five planar fractures of the infill well penetrate through Layers 2 and 3 with a height of 200 ft, and the last four planar fractures penetrate through Layers 1 through 3 with a height of 300 ft. All new fractures have no hits with pre-existing fractures. The case is designed to simulate the well-interference effect through rock matrix (Awada et al. 2016). In Case 3, the first five planar fractures are the same as those in Case 2. The last four stages of fractures are designed to have two planar fractures in each stage: One parallels the pre-existing fractures, and the other hits the pre-existing fractures with an angle. All new fractures penetrate through Layers 1 through 3 with a height of 300 ft. The upward growth of fractures in the Eagle Ford Shale Formation toward the Austin Chalk Formation is considered reasonable because the rock is more brittle in the Austin Chalk (Okeahialam et al. 2017).

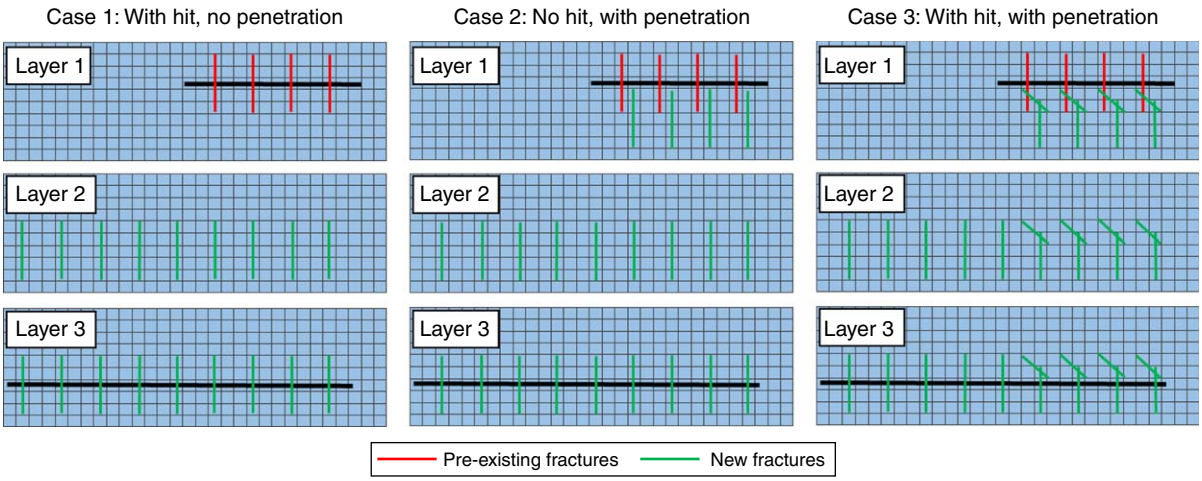

Fig. 7—Three cases of different well-interference scenarios.

A 200-day production cycle is simulated for all three well-interference cases. The infill well starts to produce when the parent well has already produced for 100 days. The wells are under the same well-control strategies as in the base case. **Figs. 8a through 8c** present the oil-production rates of parent and infill wells for the three cases. For Case 1, the oil-production rate of the parent well first increases sharply, and then it decreases below its original decline curve. It is a typical negative well-interference performance resulting from the production competition with infill wells. The sharp rate increase is mainly because of the wellbore crossflow introduced by the fracture hits. For Case 2, the producing rate of the parent well directly evolves underneath its original decline curve. The sharp rate increase cannot be observed in this case because there are no direct hits among fractures. For Case 3, the producing rate of the parent well first increases above its original decline curve, and then evolves underneath it. It is a combined result of the infill well's contribution to the SRV of the parent well and the infill well's competition with the parent well. Fig. 8d presents cumulative oil production of the parent well in all three cases and in the case without infill wells. Case 1 and Case 2 have almost the same cumulative production, which is 8.2% lower than that of the case without infill wells at the end of 200 days. Case 3 has a slightly higher cumulative production compared with the other two cases, but it is still 5.7% lower than that of the case without infill wells at the end of the production. We clearly can tell from the comparison that all three infill-well scenarios bring negative well-interference effects to the parent well in the Austin Chalk layer.

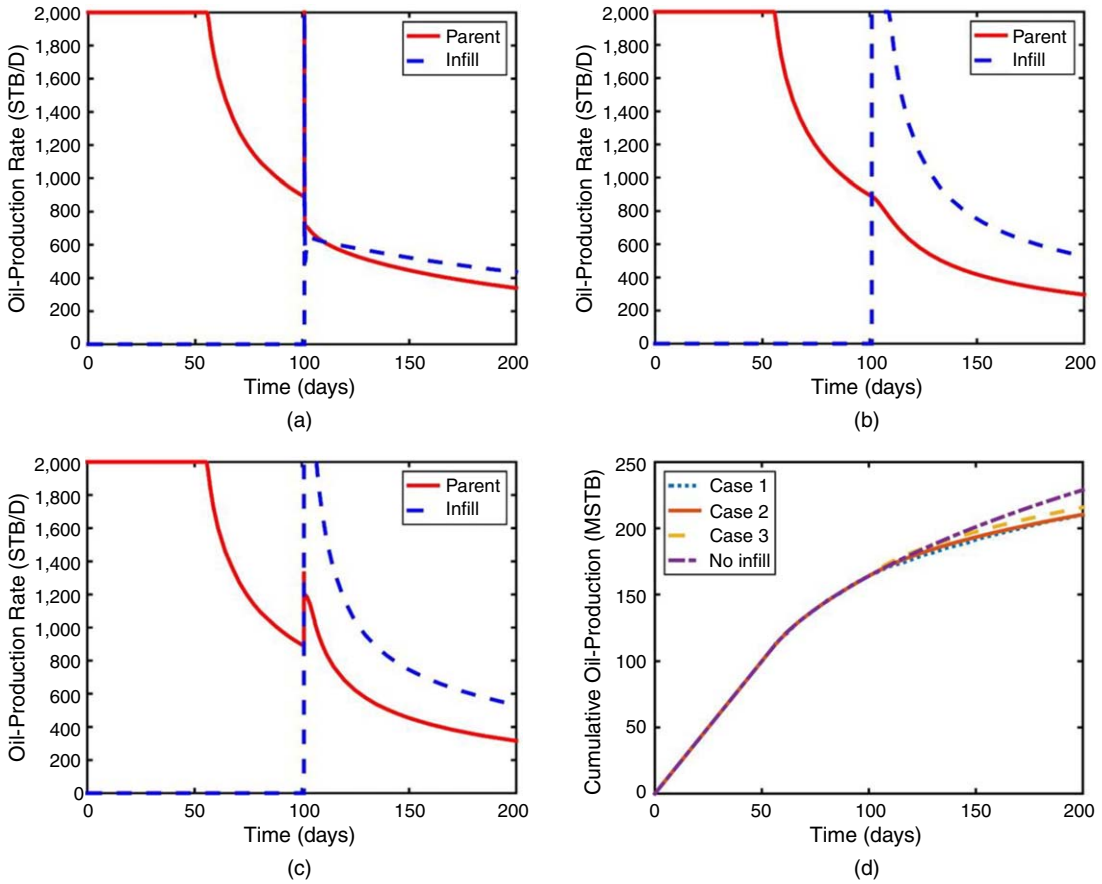

Fig. 8—(a–c) Oil-production rate of parent and infill wells for Cases 1 through 3. (d) Cumulative oil production of the parent well for Cases 1 through 3 and the case without infill wells.

Fig. 9 shows the pressure maps at the 155th day of production for the case without infill wells and the three well-interference cases. The pressure maps of Layer 1 (the Austin Chalk layer) and Layer 3 (the Eagle Ford Shale layer) are presented for each case. Both the presence of the infill well in the Eagle Ford Shale layer and the well-interference effects accelerate the pressure depletion in the Austin Chalk layer. The fracture hits in the Austin Chalk layer also accelerate the pressure depletion in the Eagle Ford Shale layer, as shown in Fig. 9d.

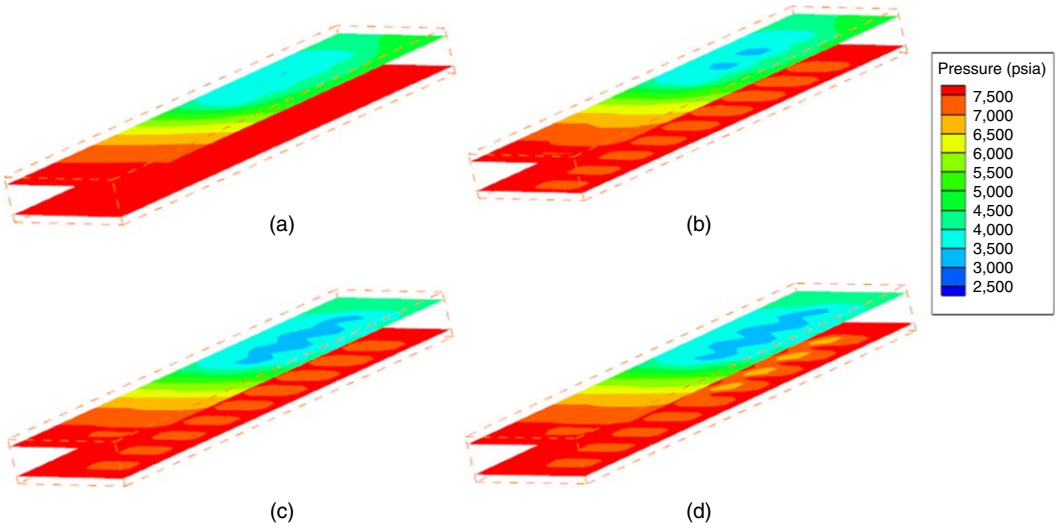

Fig. 9—Pressure maps of the case without infill wells and Cases 1 through 3 at the 155th day of production.

Effect of Reservoir Permeability. We apply Case 1 to evaluate the impact of the Eagle Ford Shale permeability on the well interference between the parent and the infill wells. A 500-day production cycle is simulated, and the infill well is brought into production at the 200th day.

Fig. 10 shows the simulation results when the Eagle Ford Shale permeability is equal to 450 nd, 0.0045 md, and 0.045 md. For the case of 450-nd permeability, the well-interference effect resembles that shown in Fig. 8a. The production of the infill well reduces the cumulative production of the parent well by 11.2% at the end of the 500-day production. For the case of 0.0045 md, the producing rate of the parent well first increases above its original decline curve after the infill well starts to produce, and then declines faster than it originally does. From the cumulative oil-production comparison, we can confirm that it is a negative well-interference scenario because the cumulative production of the parent well decreases 12.9% at the end of the 500-day production. For the case of 0.045 md, the producing rate of the parent well increases to the maximum oil-production rate of 2,000 STB/D after the infill well starts to produce. The parent well remains to produce at this rate for approximately 50 days, and then declines at a rate faster than its original decline rate because of the competition with the infill well. The cumulative oil production of the parent well at the 500th day is almost the same as that in the case without infill wells. Although we can expect a negative well-interference effect after a longer production period, the positive well-interference effect lasts for approximately 300 days in this case, which is comparable with the field observations shown in Fig. 2.

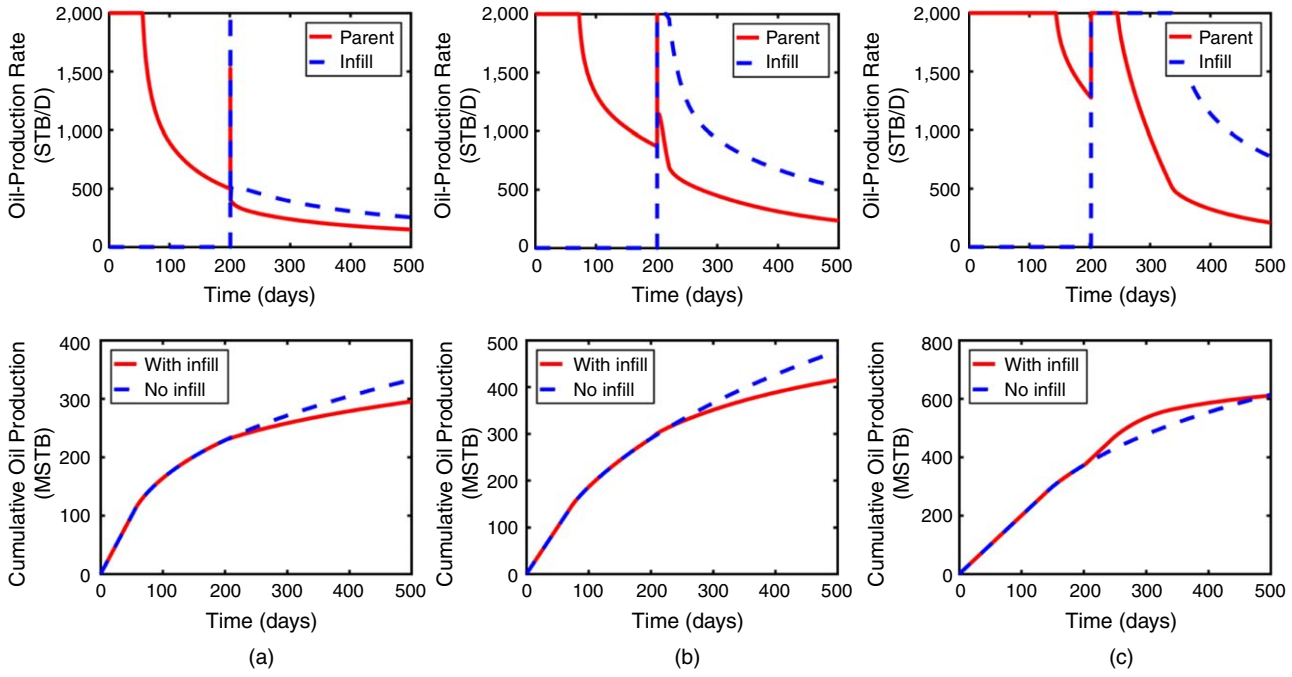

Fig. 10—Oil-production rate of the parent and infill wells and cumulative oil production of the parent well for Eagle Ford Shale permeability equal to 450 nd, 0.0045 md, and 0.045 md.

Notice that the oil-production rate of the parent well follows two decline rates after the infill well starts to produce in the cases of 0.0045- and 0.045-md permeability. It is mainly because of the different performance of the infill well under different well controls. When the infill well starts to produce, it is first under the constraint oil-production-rate control, with BHP declining quickly, which, in turn, accelerates the decline rate of the parent well. When the BHP of the infill well declines to 2,000 psi, the well control switches to the constant-BHP control, and the producing rate of the infill well starts to decline. It also results in a slower decline of the oil-production rate of the parent well.

Fig. 11 shows the pressure maps at the 250th day of production for the cases with Eagle Ford Shale permeability equal to 0.0045 and 0.045 md. The high permeability of Eagle Ford Shale leads to a faster depletion rate and a higher recovery for the Austin Chalk Formation. Therefore, if the infill well is completed in a high-permeability region of the Eagle Ford Shale Formation, the production of the infill well can lead to a positive well-interference effect for the parent well in the Austin Chalk Formation.

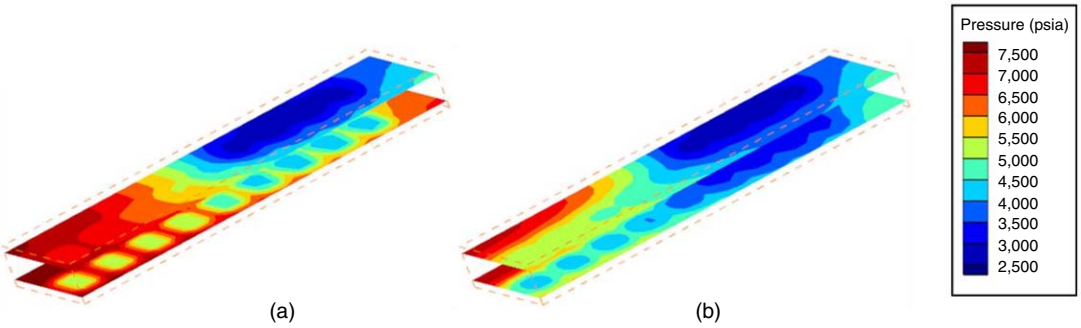

Fig. 11—Pressure maps at the 250th day of production for Eagle Ford Shale permeability equal to 0.0045 and 0.045 md.

Effect of Nanopore Confinement. In this section, we evaluate the nanopore-confinement effect of Eagle Ford Shale on the production performance of the parent and infill wells, and the well-interference effects between them. We assume that the fractures and the Austin Chalk matrix have negligible capillary pressure, whereas the Eagle Ford Shale matrix has high capillary pressure, as shown in Fig. 5. We evaluate the nanopore-confinement effect by considering capillary pressure in the phase behavior of reservoir fluid in the Eagle Ford Shale. The evaluation is based on Case 3, where the new fractures of the infill well penetrate to the upper Austin Chalk Formation and hit the existing fractures of the parent well. **Fig. 12a** shows the cumulative oil production of the parent and the infill wells with and without capillary pressure effects being considered in the VLE calculation. The two scenarios give the same cumulative oil-production curves. It is because of the extremely low permeability of the Eagle Ford Shale layer (in this case, 450 nd); most of the rock-matrix grids with no hydraulic fractures embedded do not contribute to the production. We then increase the permeability to 0.045 md, which considers the existence of natural fractures. Fig. 12b presents the cumulative oil production of the parent and the infill wells for this case. The results indicate that the cumulative oil production of the infill well increases 4.4% at the end of a 500-day production when considering the capillary pressure effect in the VLE calculation. The observation is comparable to those reported by other researchers who studied the nanopore-confinement effect on reservoir performance (Siripatrachai et al. 2017; Zhang et al. 2017b). At the same time, the cumulative oil production of the parent well decreases 3.6%. **Figs. 13a and 13b** show the oil-production rates of the parent and the infill wells with and without capillary pressure in the VLE calculation. We can observe an increase of the oil-production rate in the infill well and a drop of the oil-production rate in the parent well in the late production period. The results indicate that the consideration of the nanopore-confinement effect makes the infill well a stronger competitor in the production system. It is mainly because the additional capillary pressure in the VLE calculation leads to a lower bubblepoint pressure of a fluid mixture. In other words, the fluid properties in the Eagle Ford Shale are no longer the same as those in the Austin Chalk because of the capillary pressure in phase behavior. This situation favors the oil production of the infill well in the Eagle Ford Formation, and also leads to more negative well-interference effects for the parent well in the Austin Chalk Formation.

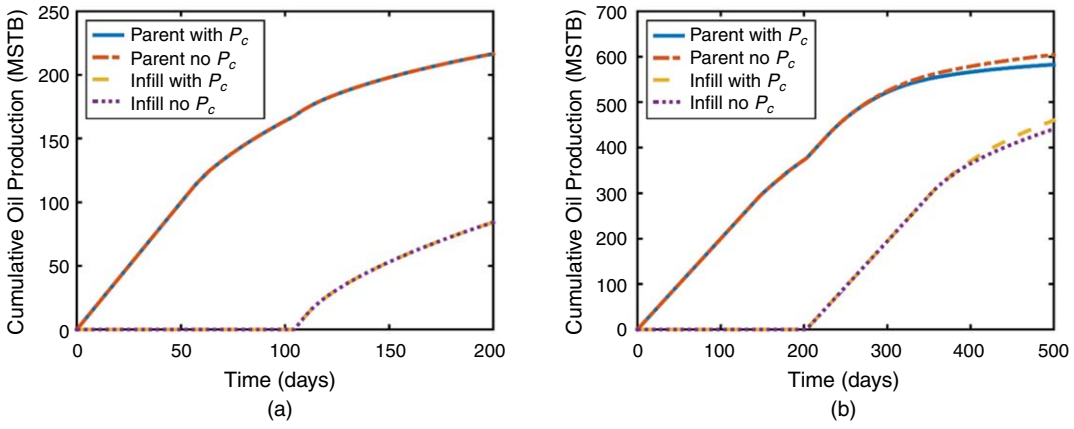

Fig. 12—Cumulative oil production of the infill and the parent wells with and without capillary pressure effects being considered in the VLE calculation for Eagle Ford layers with permeability equal to 450 nd and 0.045 md.

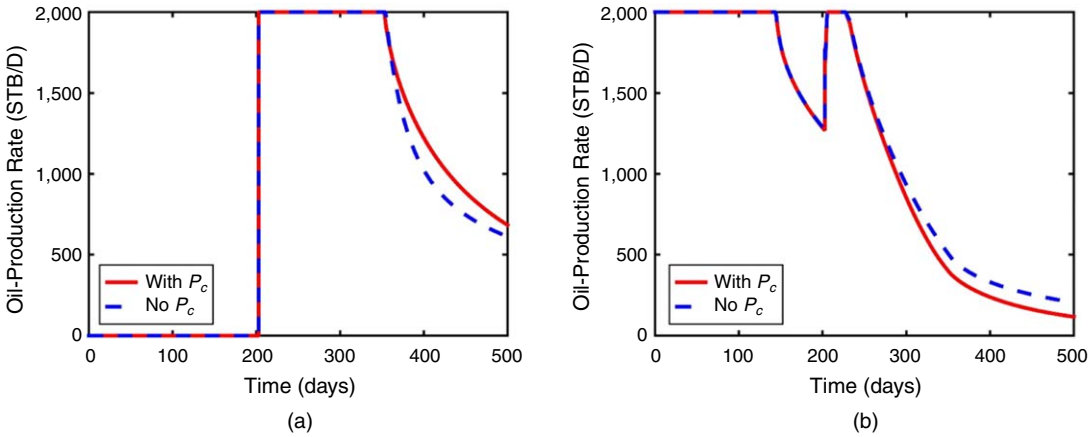

Fig. 13—Oil-production rate of the infill and the parent wells with and without capillary pressure effects being considered for permeability equal to 0.045 md.

Effect of the Hydraulic-Fracturing Process. The previous simulation results are all based on the assumption that the infill drilling and the completion process do not significantly change the reservoir properties. In the actual hydraulic-fracturing process, a large volume of fracturing fluid is injected into the formation to create fractures, and then a fracturing-fluid-flowback period will follow before the well starts to produce hydrocarbons. This process might change the reservoir pressure and water saturation, especially at the fractured zones. To account for the effect of hydraulic fracturing, we set the water saturation and the pressure of the new fracture-embedded reservoir cells to be 0.5 and 10,000 psi before the infill well starts to produce. The exact value changes must be tracked by a coupled geomechanics/reservoir model, which is beyond the scope of this paper. We investigate the impact of this synthetic hydraulic-fracturing effect on the three well-interference cases presented in Fig. 7. **Figs. 14a through 14c** present the parent-well oil-production rate of the three cases with and without the hydraulic-fracturing effect being considered. Fig. 14d shows the parent-well cumulative oil production of the three cases under the hydraulic-fracturing effect and the case without infill wells. For Case 1, where new fractures stay in the Eagle Ford Formation, the oil-production rate of the parent well does not change. For Case 2, where new fractures penetrate to the Austin Chalk Formation, the oil-production rate of the parent well increases compared with the original case. This increasing trend lasts for approximately 75 days, and then the oil-production rate goes back to its original track. The infill well in this case still brings a negative effect to the parent well at the end of the 200-day production with a 4.9% decline in cumulative oil production. For Case 3, the additional pressure brought by the infill well has a significant effect in increasing the production of the parent well because the new fractures not only penetrate to the Austin Chalk but also hit the existing fractures. Resembling Case 2, the parent-well oil-production rate drops back to its original declining track 75 days after the infill well starts to produce. In this case, the cumulative oil production of the parent well is the same as that of the no-infill case at the end of the 200-day production. Therefore, the positive well-interference effect lasts for approximately 100 days in this case, and we can expect a negative well-interference effect afterward.

Fig. 15 shows the pressure maps at the 101st day of production for Case 2 and Case 3. In both cases, the new fractures of infill wells penetrate to the Austin Chalk layer. The hydraulic-fracturing process can increase the pressure of a nearby formation, providing an additional pressure support for the existing producer. This additional pressure support can lead to a period of a positive well-interference effect for the parent well in the Austin Chalk.

Discussion

Positive and Negative Well-Interference Effects. Among all the cases being studied, only two of them show a positive well-interference effect. In one case, the Eagle Ford Shale permeability is four-times smaller than that of the Austin Chalk. In the other case, the new hydraulic fractures penetrate to the Austin Chalk Formation, and hit the existing fractures with an additional pressure support resulting from the hydraulic-fracturing process. The positive well-interference period lasts for approximately 300 days for the first case and approximately 100 days for the second case. In the field observations presented by Fig. 2, the positive well-interference period lasts for approximately 200 days, but a longer time can be expected on the basis of the rate profile. To history match these field data, a combined effect of the high-permeablility Eagle Ford Shale region and hydraulic-fracturing process can be considered.

The simulation results indicate that the negative well-interference effect is much more common for a parent well completed in the Austin Chalk Formation and in an infill well completed in the Eagle Ford Shale Formation. This conclusion makes physical sense, and coincides with field observations. However, it is not a trivial conclusion from the perspective of reservoir simulation. On the basis of our previous simulation results for 2D and 3D homogeneous reservoirs, positive well-interference results are much more commonly obtained (Tang et al. 2017a). If parent wells and infill wells are modeled in a reservoir with universal permeability, a positive well-interference result is inevitable because new fractures introduced by the infill well contribute to the SRV of the parent well. To history match the field data with negative well-interference effects, a reservoir engineer can consider setting the formation permeability around the parent wells to a significantly higher value (more than five times) than that of the surrounding formations. It is a reasonable setting when we consider the complex fracture network around the wells.

Effect of Other Reservoir Parameters. In this paper, a highly simplified reservoir model is applied to represent the Eagle Ford Shale/Austin Chalk production system. We mainly consider the differences of absolute permeability, relative permeability, and capillary pressure between the two formations. Other reservoir parameters such as initial reservoir pressure, matrix porosity, and initial water saturation are also important in differentiating the two formations. We apply the production scenario in Case 3 to study the effect of these parameters. For each parameter, we calculate the ratio of cumulative oil production at the 200th day to that of the original Case 3, as shown in **Table 3.** The first parameter is the initial reservoir pressure. Instead of applying a reservoir pressure gradient of 0.45 psi/ft, we consider the overpressure effect of the Eagle Ford Shale Formation by setting the initial reservoir pressure of the Eagle Ford layer to 9,000 and 10,000 psi, respectively. The simulation results indicate that a higher initial pressure of Eagle Ford Shale can increase the

cumulative oil production of the infill well by 5 and 10%, respectively. At the same time, the cumulative oil production of the parent well also increases by 2 and 3%. Next, we consider the effect of reservoir porosity by setting the porosity of the Eagle Ford layer to 0.05 and 0.02, respectively. The simulation results indicate that a lower-porosity Eagle Ford Shale can decrease the cumulative oil production of the infill well by 10 and 20%, but the cumulative oil production of the parent well remains almost unchanged. Finally, the effect of initial water saturation of the Eagle Ford Shale is studied. For initial water saturations equal to 0.2 and 0.1, the cumulative oil production of the infill well increases by 22 and 24%, and the cumulative oil production of the parent well increases by 5 and 6%. The oil-production-rate profiles of the two wells follow the same trends as that shown in Fig. 8c. In Table 3, we also summarize the cumulative production of the parent well when negative well interference occurs. The parent well produces 190.7 MSTB (thousand STB) of oil when the negative well interference starts in the original Case 3. For different initial reservoir pressure and porosity, the cumulative production stays at approximately 190 MSTB. However, for different initial water saturation, the cumulative production increases to 210 MSTB. The comparison reveals that the initial water saturation has the most significant impact on the well-interference effect among all the reservoir parameters being studied in this subsection.

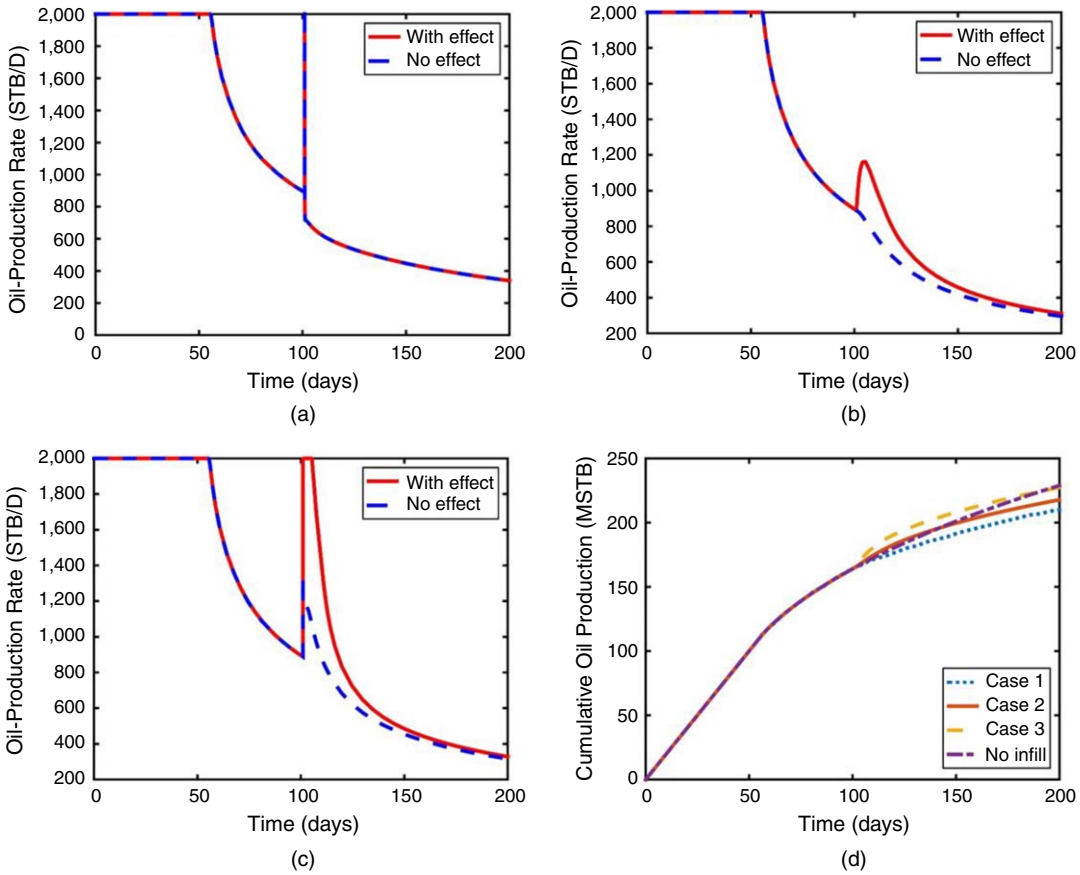

Fig. 14—(a–c) Oil-production rate of the parent and infill wells for Cases 1 through 3 with and without the hydraulic-fracturing effect. (d) Cumulative oil production of the parent well for Cases 1 through 3 with hydraulic-fracturing effect and the case without infill wells.

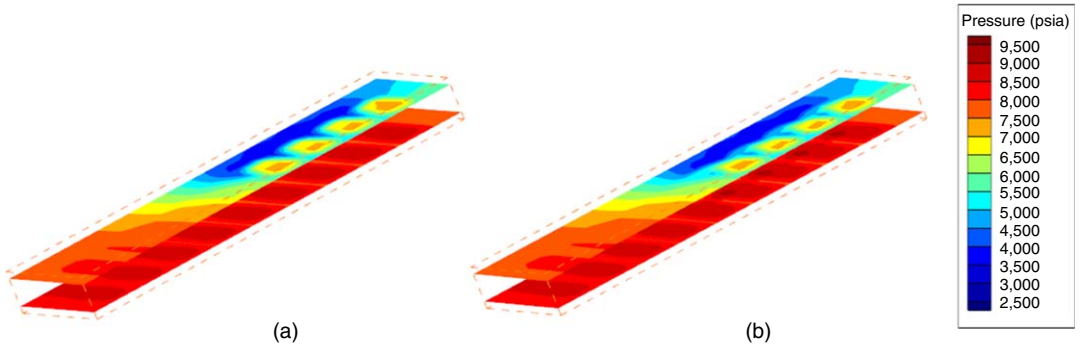

Fig. 15—Pressure maps at the 101st day of production for Case 2 and Case 3 with the additional pressure support from the hydraulic-fracturing process.

	Initial Pressure (9,000 psi)	Initial Pressure (10,000 psi)	Matrix Porosity (0.05)	Matrix Porosity (0.02)	Initial Water Saturation (0.2)	Initial Water Saturation (0.1)
Parent-well cumulative production ratio	1.02	1.03	1.00	0.99	1.05	1.06
Infill-well cumulative production ratio	1.05	1.10	0.90	0.80	1.22	1.24
Parent-well cumulative production when negative well-interference effect occurs (MSTB)	191.3	192.0	190.4	189.7	210.1	211.0

Table 3—Sensitivity analysis on other reservoir parameters.

Effect of Natural Fractures in Austin Chalk. Austin Chalk is characterized by its natural-fracture system. We analyze the effect of natural fractures by randomly generating 20 natural fractures in the Austin Chalk layer, as shown in **Fig. 16.** The properties of these fractures are shown in **Table 4.** We apply the production scenarios in Case 1 and Case 2 for analysis. The cumulative production curves of the parent well with and without natural fractures for these two cases are shown in **Fig. 17a.** At the 200th day of production, the existence of natural fractures increases the cumulative production of the parent well by 3 and 4% for Case 1 and Case 2, respectively. Fig. 17b presents the cumulative production curves of the infill well. At the 200th day of production, the cumulative production of Case 1 increases by 1%, and that of Case 2 increases by 9%. This is mainly because the fractures of the infill well penetrate to the Austin Chalk layer in Case 2. **Figs. 18a and 18b** depict the pressure maps at the 150th day of production for Case 1 and Case 2 with natural fractures. Comparing the figures with Figs. 9b and 9c, we can find that the pressure depletion becomes faster when natural fractures exist. However, the oil-production-rate profiles resemble those presented in Figs. 8a and 8b, which indicates that the production of the infill well still brings negative well-interference effects to the parent well in these two cases.

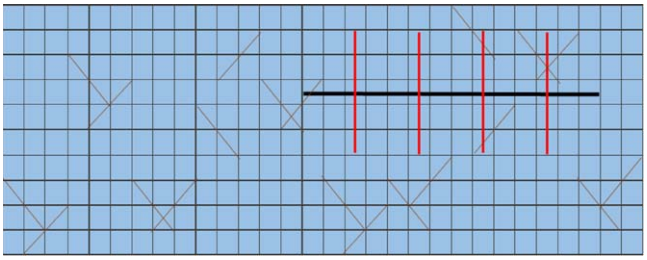

Fig. 16—Layout of the Austin Chalk layer with natural fractures embedded.

Fracture Width (ft)	Fracture Length (ft)	Fracture Permeability (md)	Fracture Porosity
0.02	282.84	3,000	1

Table 4—Properties of natural fractures.

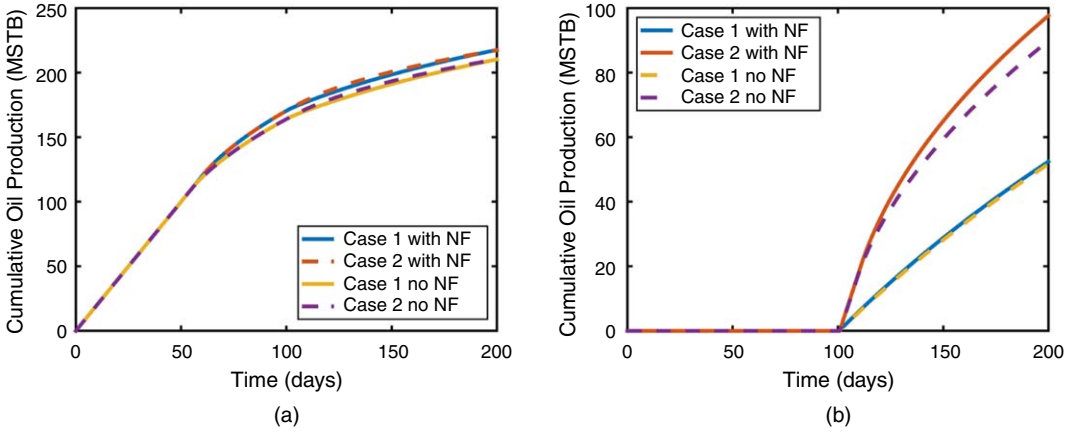

Fig. 17—Cumulative oil production of (a) the parent well and (b) the infill well with and without natural fractures (NF) being considered for Case 1 and Case 2.

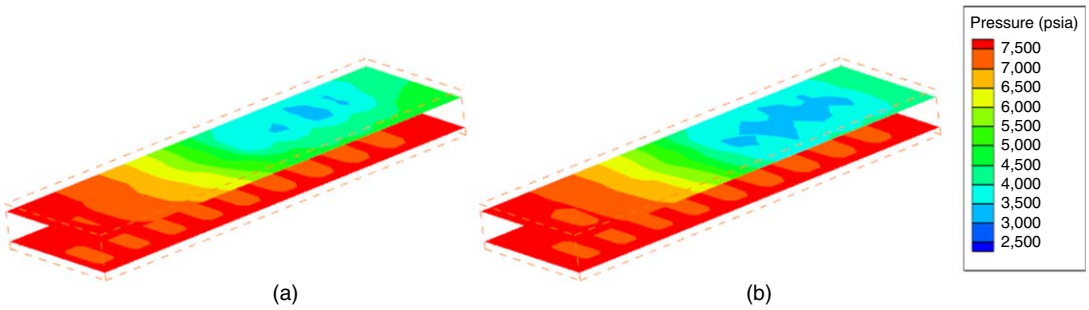

Fig. 18—Pressure maps at the 150th day of production for Case 1 and Case 2 with natural fractures in the Austin Chalk layer being considered.

Conclusions

In this study, we investigated the well-interference phenomenon in two different formations with a compositional reservoir model for the first time. The newly developed compositional reservoir model considered the nanopore-confinement effect in phase behavior and applied an EDFM to simulate the new fractures introduced by infill wells. We also included the multisegment-wellbore model to characterize the wellbore crossflow introduced by fracture hits. The model was validated against a commercial reservoir simulator, with excellent agreement.

We specifically focused on studying the effect of an infill well in the Eagle Ford Shale Formation on the production performance of a parent well in the Austin Chalk Formation. Different reservoir properties and hydraulic-fracturing impacts were evaluated through the reservoir model. The following conclusions are obtained from the simulation results:

- The multisegment-well model allows the program to characterize the wellbore crossflow introduced by fracture hits. The simulation results also prove that the sharp production-rate increase of parent wells can be an indicator of direct fracture hits between parent and infill wells.
- Infill wells in Eagle Ford Shale most likely result in negative impacts on existing producers in Austin Chalk. From the perspective of reservoir simulation, the main parameter that contributes to the phenomenon is the reservoir-permeability difference between the two formations.
- A smaller permeability difference between the two formations and the additional pressure support caused by hydraulic fracturing can lead to positive well-interference effects for the parent well after the infill well starts to produce. This positive well-interference period can last for several hundred days.
- The nanopore-confinement effect can lead to more negative well-interference impacts on the parent well in Austin Chalk if the permeability of the Eagle Ford Shale region is sufficiently large.

For future work, the model can be extended to incorporate the geomechanical model, under which circumstance the effect of hydraulic fracturing and fracture geometries can be evaluated more rigorously. Although the reservoir-permeability difference shows a significant impact on the positive and negative well-interference effects within the scope of this paper, we acknowledge that it should not be the only reason because of the complexity of the well-interference phenomenon. Other potential reasons are not limited to reservoir geology (faults or overpressure), well completions (fracture counts and quality), and depletion strategies.

Nomenclature

A = cross-section of the flow path, ft^2
k = permeability
K = equilibrium ratio
M = net molar flow rate from each perforation, lbmol/sec
N = moles per unit volume, lbmol/ft^3
P = pressure, psia
S = saturation
u = fluid velocity in wellbore, ft/sec
V = volume, ft^3
w = acentric factor
x = mole fraction in oil phase
y = mole fraction in gas phase
z = overall mole fraction
Z = compressibility factor
κ = binary interaction coefficient
μ = viscosity, cp
ρ_m = bulk mixture density, lb/ft^3
$\rho_{m\alpha}$ = molar density of phase α, lbmol/ft^3
ϕ = porosity
φ = fugacity coefficient
Ψ = phase potential, psia

Subscripts

c = hydrocarbon component
g = gas
l = liquid
m = mixture
o = oil
w = water

Acknowledgments

The authors would like to express their appreciation for financial support from the Crisman Institute for Petroleum Research at Texas A&M University.

References

Agboada, D. K. and Ahmadi, M. 2013. Production Decline and Numerical Simulation Model Analysis of the Eagle Ford Shale Play. Presented at the SPE Western Regional and AAPG Pacific Section Meeting 2013 Joint Technical Conference, Monterey, California, 19–25 April. SPE-165315-MS. https://doi.org/10.2118/165315-MS.

Ajani, A. A. and Kelkar, M. G. 2012. Interference Study in Shale Plays. Presented at the SPE Hydraulic Fracturing Technology Conference, The Woodlands, Texas, 6–8 February. SPE-151045-MS. https://doi.org/10.2118/151045-MS.

Awada, A., Santo, M., Lougheed, D. et al. 2016. Is That Interference? A Work Flow for Identifying and Analyzing Communication Through Hydraulic Fractures in a Multiwell Pad. *SPE J*. **21** (5): 1554–1566. SPE-178509-PA. https://doi.org/10.2118/178509-PA.

Cao, H. 2002. *Development of Techniques for General Purpose Simulators*. PhD dissertation, Stanford University, Stanford, California.

Chai, Z., Yan, B., Killough, J. E. et al. 2018. An Efficient Method for Fractured Shale Reservoir History Matching: The Embedded Discrete Fracture Multi-Continuum Approach. *J. Pet. Sci. Eng*. **160:** 170–181. https://doi.org/10.1016/j.petrol.2017.10.055.

Energy Information Agency. 2010. Eagle Ford Shale Play, Western Gulf Basin, South Texas, http://www.eia.gov/oil_gas/rpd/shaleusa9.pdf (accessed September 21, 2017).

Fjar, E., Holt, R. M., Raaen, A. M. et al. 2008. *Petroleum-Related Rock Mechanics*. Elsevier.

He, Y., Cheng, S., Li, S. et al. 2017. A Semianalytical Methodology To Diagnose the Locations of Underperforming Hydraulic Fractures Through Pressure-Transient Analysis in Tight Gas Reservoir. *SPE J*. **22** (3): 924–939. SPE-185166-PA. https://doi.org/10.2118/185166-PA.

Hentz, T. F. and Ruppel, S. C. 2010. Regional Lithostratigraphy of the Eagle Ford Shale: Maverick Basin to East Texas Basin. *Gulf Coast Assoc. Geol. Soc. Trans*. **60:** 325–337.

Holmes, J. 1983. Enhancements to the Strongly Coupled, Fully Implicit Well Model: Wellbore Crossflow Modeling and Collective Well Control. Presented at the SPE Symposium on Reservoir Simulation, San Francisco, 15–18 November. SPE-12259-MS. https://doi.org/10.2118/12259-MS.

Hovorka, S. D. 1998. Facies and Diagenesis of the Austin Chalk and Controls on Fracture Intensity—A Case Study From North Central Texas. The University of Texas at Austin, Bureau of Economic Geology, Geological Circular 98-2, 47 p.

Jia, P., Cheng, L., Clarkson, C. R. et al. 2017. A Laplace-Domain Hybrid Model for Representing Flow Behavior of Multifractured Horizontal Wells Communicating Through Secondary Fractures in Unconventional Reservoirs. *SPE J*. **22** (6): 1856–1876. SPE-186109-PA. https://doi.org/10.2118/186109-PA.

Jiang, J. and Younis, R. M. 2017. An Improved Projection-Based Embedded Discrete Fracture Model (Pedfm) for Multiphase Flow in Fractured Reservoirs. *Adv. Water Resour*. **109:** 267–289. https://doi.org/10.1016/j.advwatres.2017.09.017.

Kou, R., Alafnan, S. F. K., and Akkutlu, I. Y. 2017. Multi-Scale Analysis of Gas Transport Mechanisms in Kerogen. *Transport in Porous Media* **116** (2): 493–519.

Kurtoglu, B. and Salman, A. 2015. How To Utilize Hydraulic-Fracture Interference to Improve Unconventional Development. Presented at the Abu Dhabi International Petroleum Exhibition and Conference, Abu Dhabi, 9–12 November. SPE-177953-MS. https://doi.org/10.2118/177953-MS.

Liu, Q., Tian, S., Li, G. et al. 2018. An Analytical Model for Fracture Initiation From Radial Lateral Borehole. *Journal of Petroleum Science and Engineering* **164** (May): 206–218. https://doi.org/10.1016/j.petrol.2018.01.056.

Marongiu-Porcu, M., Lee, D., Shan, D. et al. 2016. Advanced Modeling of Interwell-Fracturing Interference: An Eagle Ford Shale-Oil Study. *SPE J*. **21** (5): 1567–1582. SPE-174902-PA. https://doi.org/10.2118/174902-PA.

Martin, R., Baihly, J. D., Malpani, R. et al. 2011. Understanding Production From Eagle Ford-Austin Chalk System. Presented at the SPE Annual Technical Conference and Exhibition, Denver, 30 October–2 November. SPE-145117-MS. https://doi.org/10.2118/145117-MS.

Moinfar, A. 2013. *Development of an Efficient Embedded Discrete Fracture Model for 3D Compositional Reservoir Simulation in Fractured Reservoirs*. PhD dissertation, The University of Texas at Austin, Austin, Texas (August 2013).

Nojabaei, B., Johns, R. T., Chu, L. et al. 2013. Effect of Capillary Pressure on Phase Behavior in Tight Rocks and Shales. *SPE Res Eval & Eng* **16** (3): 281–289. SPE-159258-PA. https://doi.org/10.2118/159258-PA.

Okeahialam, I., Yang, M., Shinde, D. B. et al. 2017. Completion Optimization Under Constraints: An Eagle Ford Shale Case Study. *SPE Prod & Oper* **32** (2): 128–136. SPE-174057-PA. https://doi.org/10.2118/174057-PA.

Pearson, K. 2010. Geologic Controls on Austin Chalk Oil and Gas Production: Understanding a Dual Conventional-Continuous Accumulation. *Gulf Coast Assoc. Geol. Soc. Trans*. **60:** 557–570.

Peng, D.-Y. and Robinson, D. B. 1976. A New Two-Constant Equation of State. *Ind. Eng. Chem. Fundam.* **15** (1): 59–64. https://doi.org/10.1021/i160057a011.

Sahai, V., Jackson, G., Lawal, H. et al. 2015. A Quantitative Approach To Analyze Fracture-Area Loss in Shale Gas Wells During Field Development and Restimulation. *SPE Res Eval & Eng* **18** (3): 346–355. SPE-169406-PA. https://doi.org/10.2118/169406-PA.

Siripatrachai, N., Ertekin, T., and Johns, R. T. 2017. Compositional Simulation of Hydraulically Fractured Tight Formation Considering the Effect of Capillary Pressure on Phase Behavior. *SPE J*. **22** (4): 1046–1063. SPE-179660-PA. https://doi.org/10.2118/179660-PA.

Stone, H. L. 1973. Estimation of Three-Phase Relative Permeability and Residual Oil Data. *J Can Pet Technol* **12** (4): 53–61. PETSOC-73-04-06. https://doi.org/10.2118/73-04-06.

Stone, T., Edmunds, N., and Kristoff, B. 1989. A Comprehensive Wellbore/Reservoir Simulator. Presented at the SPE Symposium on Reservoir Simulation, Houston, 6–8 February. SPE-18419-MS. https://doi.org/10.2118/18419-MS.

Tang, H., Chai, Z., Yan, B. et al. 2017a. Application of Multi-Segment Well Modeling To Simulate Well Interference. Presented at the SPE/AAPG/SEG Unconventional Resources Technology Conference, Austin, Texas, 24–26 July. URTEC-2668100-MS. https://doi.org/10.15530/URTEC-2017-2668100.

Tang, H., Killough, J. E., Heidari, Z. et al. 2017b. A New Technique To Characterize Fracture Density by Use of Neutron Porosity Logs Enhanced by Electrically Transported Contrast Agents. *SPE J*. **22** (4): 1034–1045. SPE-181509-PA. https://doi.org/10.2118/181509-PA.

Tunstall, T. 2015. Iterative Bass Model Forecasts for Unconventional Oil Production in the Eagle Ford Shale. *Energy* **93:** 580–588. https://doi.org/10.1016/j.energy.2015.09.072.

Valbuena Olivares, E. 2015. *Production Performance Modeling Through Integration of Reservoir and Production Network With Asphaltene Deposition*. PhD dissertation, Texas A&M University, College Station, Texas.

Walls, J. D. and Sinclair, S. W. 2011. Eagle Ford Shale Reservoir Properties From Digital Rock Physics. *First Break* **29** (6): 97–101.

Xu, Y., Cavalcante Filho, J. S. A., Yu, W. et al. 2017. Discrete-Fracture Modeling of Complex Hydraulic-Fracture Geometries in Reservoir Simulators. *SPE Res Eval & Eng* **20** (2): 403–422. SPE-183647-PA. https://doi.org/10.2118/183647-PA.

Yan, B. 2017. *Development of General Unstructured Reservoir Utility and Fracture Reservoir Modeling*. PhD dissertation, Texas A&M University, College Station, Texas.

Yan, B., Wang, Y., and Killough, J. E. 2017. A Fully Compositional Model Considering the Effect of Nanopores in Tight Oil Reservoirs. *J. Pet. Sci. Eng.* **152:** 675–682. https://doi.org/10.1016/j.petrol.2017.01.005.

Yu, W., Xu, Y., Weijermars, R. et al. 2018. A Numerical Model for Simulating Pressure Response of Well Interference and Well Performance in Tight Oil Reservoirs With Complex-Fracture Geometries Using the Fast Embedded-Discrete-Fracture-Model Method. *SPE Res Eval & Eng* **21** (2): 489–502. SPE-184825-PA. https://doi.org/10.2118/184825-PA.

Zhang, Y., Lashgari, H. R., Di, Y. et al. 2017a. Capillary Pressure Effect on Phase Behavior of CO_2/Hydrocarbons in Unconventional Reservoirs. *Fuel* **197:** 575–582. https://doi.org/10.1016/j.fuel.2017.02.021.

Zhang, Y., Yu, W., Sepehrnoori, K. et al. 2017b. A Comprehensive Numerical Model for Simulating Fluid Transport in Nanopores. *Scientific Reports* **7**. https://doi.org/10.1038/srep40507.

Appendix A

Here, we list the definitions of parameters in Eq. 12. The compressibility factor Z is solved by finding the cubic root of the Peng-Robinson EOS (Peng and Robinson 1976),

$$Z_\alpha^3 - (1 - B_\alpha)Z_\alpha^2 + (A_\alpha - 3B_\alpha^2 - 2B_\alpha)Z_\alpha - (A_\alpha B_\alpha - B_\alpha^2 - B_\alpha^3) = 0, \quad \text{(A-1)}$$

where

$$A_\alpha = \frac{P_\alpha a}{(RT)^2}, \quad \text{(A-2)}$$

$$B_\alpha = \frac{P_\alpha b}{RT}, \quad \text{(A-3)}$$

$$a = \sum_{c=1}^{n_c}\sum_{j=1}^{n_c} x_c x_j (1 - \kappa_{cj})\sqrt{a_c a_j}, \quad \text{(A-4)}$$

$$b = \sum_{j=1}^{n_c} x_j b_j, \quad \text{(A-5)}$$

$$a_j = 0.4572\frac{(RT_{cj})^2}{P_{cj}}\left[1 + m_j\left(1 - \sqrt{T/T_{cj}}\right)\right]^2, \quad \text{(A-6)}$$

$$b_j = 0.0778\frac{RT_{cj}}{P_{cj}}, \quad \text{(A-7)}$$

$$m_j = 0.3746 + 1.5423w_j - 0.2699w_j^2 \quad (w_j < 0.49),$$
$$m_j = 0.3796 + 1.4850w_j - 0.1644w_j^2 + 0.0167w_j^3 \quad (w_j \geq 0.49), \quad \text{(A-8)}$$

where κ_{cj} is the binary-interaction coefficient between components c and j, w_j is the acentric factor of component j, and T_{cj} and P_{cj} are critical temperature and critical pressure of component j.

Hewei Tang is a PhD-degree candidate in the Petroleum Engineering Department at Texas A&M University. Her research interests include reservoir-simulator development, coupled wellbore/reservoir simulation, wellbore multiphase-flow modeling, and reservoir characterization. Tang holds a BS degree in chemical engineering from Tsinghua University, China, and an MS degree in petroleum engineering from Texas A&M University. She is a member of SPE.

Bicheng Yan is currently a reservoir engineer at Sanchez Oil and Gas Corporation. Previously, he worked as a reservoir-simulation engineer at ConocoPhillips. Yan's research interests include compositional reservoir-simulator development, efficient fractured-reservoir characterization, fluid flow, and phase behavior in nanoshale, and the integrated-reservoir-modeling approach for unconventional reservoirs. He has authored or coauthored more than 40 technical papers. Yan holds a PhD degree in petroleum engineering from Texas A&M University.

Zhi Chai is currently a PhD-degree student at Texas A&M University. His research interests include fractured-reservoir simulation, assisted history matching, and uncertainty quantification. Chai holds an MS degree from Peking University in geoscience, and a BS degree in petroleum engineering from China University of Petroleum, Beijing. He is a member of SPE.

Lihua Zuo is a post-doctoral-degree researcher in the Department of Petroleum Engineering at Texas A&M University. His research interests include inverse problems, analytical and numerical streamline-based methods, decline-curve analysis, production forecast using fractional diffusion equations, semianalytical methods, and fracture modeling in shale gas and tight oil reservoirs. Zuo holds a PhD degree in applied mathematics from Texas A&M University, and an MS degree from Fudan University and a BS degree from Nanjing University of Science and Technology in applied mathematics. He is an SPE member.

John Killough is a professor in the Petroleum Engineering Department at Texas A&M University. Previously, he was a Technology Fellow for reservoir simulation at Halliburton. Killough's research interests include reservoir simulation and high-performance computing. He has authored more than 50 technical papers, and holds three patents. Killough holds a PhD degree in mathematical sciences from Rice University.

Zhuang Sun is a PhD-degree candidate in petroleum and geosystems engineering at the University of Texas at Austin. He holds a BS degree in chemical engineering from Tsinghua University. Sun's research interests include CO_2 sequestration, rock mechanics, and hydraulic-fracture modeling using coupled computational fluid dynamics and the discrete-element method. He has authored or coauthored more than 10 technical papers. Sun is a member of SPE.